STRUCTURAL, MAGNETIC AND OPTICAL PROPERTIES OF $Co_{0.5}Ni_{0.5}Fe_2O_4$ NANOPARTICLES SYNTHESIZED BY SOL-GEL AUTO COMBUSTION METHOD

A. M. MOHAMMAD[a,*], M. M. MOHAMMED[b], L.A. HUSSEIN[c]
[a]*University of Garmian, College of Education, Department of Physics, Kurdistan region, Iraq.*
[b]*University of Garmian, College of Education, Department of Chemistry, Kurdistan region, Iraq*
[c]*Baghdad University, College of Science, Department of Astronomy and Space, Baghdad, Iraq*

In the present study, $Co_{0.5}Ni_{0.5}Fe_2O_4$ ferrite nanoparticles have been synthesized using sol-gel auto combustion method. The effects of calcination temperature on structural, magnetic and optical properties have been investigated. X-ray diffraction (XRD) and fourier transform infrared spectroscopy (FT-IR) have confirmed the formation of a spinal type of ferrite structure. The average crystallite size of the ferrite samples was between 43.672 and 61.795 nm, which was found to be dependent on the calcination temperature. Morphology studies demonstrated by field emission scanning electron microscopy (FE-SEM) showed that the grain size increases as the calcination temperature increase. Energy dispersive spectrum (EDS) has also confirmed the presence of Co, Ni, Fe, and O in all samples. The band-gap energy (E_g) has been evaluated using diffuse reflectance spectra (DRS). As the calcination increased, the E_g decreased from 2.388 to 2.055 eV. Furthermore, magnetization measurements for the as-burnt and calcined samples were measured by a vibrating sample magnetometer (VSM), the results showed ferrimagnetic behavior for all samples. Saturation magnetization (M_S) increases from 46.1291 to 61.5354 emu/g as the calcination temperature increase. This behavior is related to spin canting and disorder in the surface spin, meanwhile, coercivity values (H_c) of all ferrite samples decrease from 1595 to 558.15 Oe with the increase of the calcination temperature. The squareness ratio (S) lies between 0.50 and 0.56 and the nanoparticles have exchange-coupled interaction.

(Received October 19, 2019; Accepted March 20, 2020)

Keywords: Ferrites nanoparticle, Optical properties, Sol-Gel auto combustion method

1. Introduction

Due to their excellent magnetic and electrical properties, spinel as a kind of ferrites materials has been in the forefront of nanoscience and nanotechnology. The ability of the ferrite to distribute cations between tetrahedral and octahedral sites is the basic property that makes it possess interesting physical and chemical properties [1]. Spinel cobalt ferrite $CoFe_2O_4$ is considered as a temperate hard ferromagnetic material and has properties of an inverse spinel structure which depends on thermal treatment and preparation conditions. It has such essential properties as moderate saturation magnetization, high magneto-crystalline anisotropy, and high magnetic sensitivity [2]. Nickel ferrite $NiFe_2O_4$ also has an inverse spinel structure and is considered one of the significant kinds of the spinel ferrites. Because of its high resistance, Nickel ferrite is suitable for a number of applications, especially in high-frequency. Nickel ferrite displaying ferrimagnetism properties originates from the magnetic moment of anti-parallel spins between Fe^{3+} and Ni^{2+} ions at tetrahedral and octahedral sites respectively [3, 4]. The incorporation of different metal ions (divalent or tetravalent) into $CoFe_2O_4$ lattice may alter several properties of the host. Due to the change in the initial structure, the substitution of magnetic or nonmagnetic ions in cobalt ferrite induces strain which presumably changes their characteristics significantly. Additional factors such as heat treatment, preparation mechanism, substituent, and cation

*Corresponding author: ali.mustafa@garmian.edu.krd

distribution in the two tetrahedral and octahedral sites are also responsible for the final properties [5]. The preparation method may play a remarkable role in the structure and morphology properties of the spinel ferrites. Various methods, such as the co-precipitation [6], hydrothermal [7], micro-emulsion routes [8], sol gel combustion method [9], have been developed to prepare ferrite nanoparticles. In the present study, $Co_{0.5}Ni_{0.5}Fe_2O_4$ nanoparticles were synthesized by sol-gel auto combustion method. The effect of calcination temperature on structural, magnetic and optical properties was investigated.

2. Experimental details

2.1. Synthesis

Stoichiometric formula of cobalt-nickel ferrite nanoparticles $Co_{0.5}Ni_{0.5}Fe_2O_4$ were synthesized using sol-gel auto combustion method. The solution containing desired stoichiometric amount of nitrates of Co, Ni, and Fe was mixed with citric acid in a molar ratio 1:1. Solution pH was made neutral ~7 by adding a dilute ammonia solution. The solution was stirred at 80 °C on a magnetic stirrer until the solution became dense and eventually converted into a gel. The final gel was heated to 285 °C to initiate a self-combustion reaction and produce as-burnt ferrite powder. The as-burnt ferrite samples were then calcined at various temperatures of 500, 600, 700, and 800 °C for 3 hours in a furnace to obtain monophasic $Co_{0.5}Ni_{0.5}Fe_2O_4$ spinel ferrite.

2.2. Characterizations

The crystalline phases of synthesized powders were studied using X-Ray Diffraction (XRD), model PANalytical (X'pert Pro, Netherlands) equipped with Cu kα radiation source (λ= 0.154 nm, 40 mA, and 40 kV). The morphology of the ferrite samples was investigated by field emission scanning electron microscopy (FE-SEM), using (FE-SEM; Model Mira3-XMU, TESCAN, japan). Fourier transform infrared spectroscopy for all the samples have been recorded using a Perkin Elmer FT-IR spectrometer, USA, in the range 400 to 3000 cm^{-1} using KBr pellets to ratify the spinel structure of the samples. Optical band-gab energy of the samples was determined by using diffuse reflectance spectroscopy (DRS) (Avantes spectrophotometer, model Avaspec-2048; Netherlands). The magnetic properties of all samples have been carried out by means of vibrating sample magnetometer (VSM), using a (LBKFB model Meghnatis Daghigh Kavir Company) at room temperature.

3. Results and discussion

3.1. XRD analysis

X-ray diffraction patterns of $Co_{0.5}Ni_{0.5}Fe_2O_4$ ferrite samples (as-burnt, 500, 600, 700, and 800 °C) are shown in Fig. 1. The X-ray patterns of all ferrite samples confirmed the formation of the single-phase spinel structure, and no diffraction peaks from other impurities were observed which indicates the high purity of the products. All samples showed the reflection peaks from the plains (111), (220), (311), (222), (400), (422), (511), and (440) which can be indexed to $CoFe_2O_4$ and $NiFe_2O_4$ according to the standard ICSD cards [00-001-1121] and [98-006-0930] respectively.

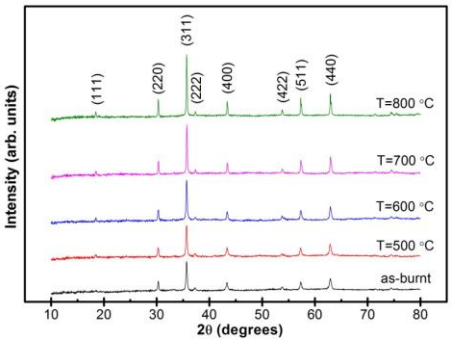

Fig. 1. X-ray diffraction pattern of $Co_{0.5}Ni_{0.5}Fe_2O_4$ nanoferrites for as-burnt and different calcination temperature (500, 600, 700, and 800 °C).

The crystallinity of the ferrite nanoparticles products was highly sensitive to the change of the calcination temperature. Broad XRD peaks for the as-burnt sample were observed. This very peak broadening suggests a poor growth of the ferrite nanoparticles structure while with the increase of the calcination temperature, sharper and more intense peaks found which can be due to the grain growth of the particles [10].

The crystallite sizes (D) of spinel samples were calculated using Scherrers formula. Given the main diffraction peak of cubic spinel ferrite at (311) plane, the lattice parameter (a), X-ray density (ρ_x) and the hopping length (L_A) and (L_B) at tetrahedral and octahedral site respectively were calculated from the relations given below [11].

$$D = \frac{0.9\,\lambda}{\beta \cos\theta} \tag{1}$$

$$a = d_{hkl}\sqrt{h^2 + k^2 + l^2} \tag{2}$$

$$\rho_x = \frac{8M}{Na^3} \tag{3}$$

$$L_A = 0.25\,a\,\sqrt{3} \tag{4}$$

$$L_B = 0.25\,a\,\sqrt{2} \tag{5}$$

where λ is the X-ray wavelength, β is the full width of the diffraction line at half maximum of the concerned peak, d is the interplanar distance, (h, k, l) are the miller indices, M is molecular weight, and N is avogadro number. The average crystallite size varied from 43.672 to 61.795 nm as the calcination temperature increased from as-burnt to 800 ˚C, respectively (Fig. 1 and Table 1). The value of the 'a' lattice parameter evaluated from the XRD spectra is in the range of approximately 8.329-8.348 nm. In our $Co_{0.5}Ni_{0.5}Fe_2O_4$ nanoparticles, it is observed that the lattice parameter decreases with increasing calcinations temperature, this result well agreed with the earlier reports [12]. The x-ray density (ρ_x) depends on the lattice parameter, and it was observed as the calcination temperature increases, the value of x-ray density decreases. The gradual decrease in the hopping length (L_A) in sites A and (L_B) in sites B between the magnetic ions (Table 1) with the increase of the calcination temperature can be explained on the basis of the decrease in the lattice parameter.

Table 1. Crystallite size (D), Lattice parameter 'a', X-ray density (ρ_x), hopping length (L_A) and (L_B) of $Co_{0.5}Ni_{0.5}Fe_2O_4$ nanoferrites for as-burnt and different calcination temperature (500, 600, 700, and 800 °C).

Temp.°C	***D*(nm)**	***a*(Å)**	**ρ_x(gm/cm^3)**	**d_A(Å)**	**d_B(Å)**
as-burnt	43.672	8.348	5.354	3.6148	2.9515
500	46.087	8.344	5.361	3.6132	2.9501
600	47.943	8.342	5.366	3.6121	2.9492
700	51.500	8.332	5.384	3.6080	2.9459
800	61.795	8.329	5.391	3.6066	2.9447

3.2. Fourier transform infrared spectroscopy (FT-IR) analysis

The FT-IR spectrum study is the most significant apparatus used to obtain information about the position of the ions in the crystal structure based on the vibrational modes [11]. The FT-IR spectrums of all the synthesized samples are illustrated in Fig. 2. It is observed that the two principal absorption bands below 1000 cm^{-1} correspond to the vibrational modes of all the spinel compounds. The occurrence of the band in the range of 585.92 to 616.25 cm^{-1} (high frequency ν_1) corresponds to the vibration of tetrahedral metal-oxygen ($M_{tetra} \leftrightarrow O$) bond, whereas that in the range of 414.85 to 477.35 cm^{-1} (low frequency ν_2) arises due to the intrinsic vibrations of metal-oxygen ($M_{octa} \leftrightarrow O$) bond at octahedral sites. The positions of band ν_1 and ν_2 as a function of the calcination temperature are listed in Table 2. Frequency variation between the ν_1 and ν_2 may be due to the long bond length of the (O-M) ions in the octahedral sites and the shorter bond length of the (O-M) ions in the tetrahedral sites [13]. In the present work, infrared spectra of all samples exhibit the characteristics of the ferrite absorption bands, confirming the formation of the cubic spinel structure.

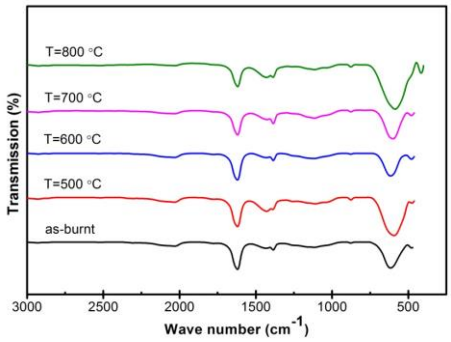

Fig. 2. FT-IR spectra of $Co_{0.5}Ni_{0.5}Fe_2O_4$ nanoferrites for as-burnt and different calcination temperature (500, 600, 700, and 800 °C).

Similar trend in shifting of peaks is seen for the bands ν_1 towards the lower frequencies side with the increase of the calcined temperatures (500, 600, 700, and 800 °C) and unambiguously depicts a mixed spinel state of $Co_{0.5}Ni_{0.5}Fe_2O_4$, which can be related to the change in the bond lengths between metal ions located on the tetrahedral and octahedral sites and oxygen ions.

Table 2. Wave-number obtained from FT-IR spectroscopy of $Co_{0.5}Ni_{0.5}Fe_2O_4$ nanoferrites for as-burnt and different calcination temperature (500, 600, 700, and 800 °C).

Temp.°C	***FTIR frequency bands*** **(cm^{-1})**	
	v_1	v_2
as-burnt	616.25	477.35
500	572.44	475.31
600	615.86	478.16
700	600.10	478.66
800	585.92	414.85

An absorption band at 1620 and 1400 cm^{-1} is shown by all samples, corresponding to the stretching vibration of carboxyl group and the presence of traces of NO_3^- ions, respectively. The bands at 825 cm^{-1} correspond to the vibration deformation of C–H group [14].

3.3. Morphology and Elemental analysis

The FE-SEM images of as-burnt and calcined samples at 600 and 800 °C, were analyzed to understand the effect of the calcination temperature on the morphology of $Co_{0.5}Ni_{0.5}Fe_2O_4$ compound and are presented in Fig. 3 (a-c).

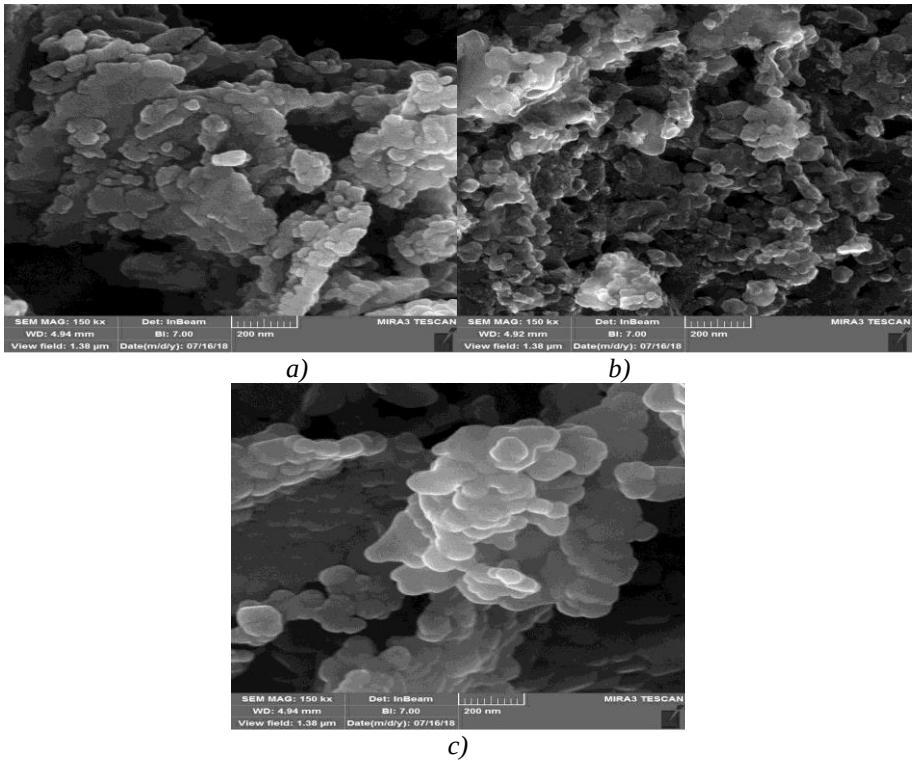

a) *b)*

c)

Fig. 3. FE-SEM images of $Co_{0.5}Ni_{0.5}Fe_2O_4$ nanoferrites for (a) as-burnt (b) calcined sample at 600 ^oC and (c) calcined at 800 ^oC.

All samples show the grain agglomeration, which is perhaps because of the calcination temperature [15], or/and is the result of magnetic interaction between nanoparticles [16]. FE-SEM images revealed that the samples have displayed an aggregate with large intergranular porosity. The apparent holes attribute to various gas amounts emitted through combustion [17]. The particle size obtained by FE-SEM images is slightly larger than that determined by XRD. Fig. 3(a-c)

shows a uniform distribution of nanoparticles with a mean size 51.564, 58.092, and 86.020 nm for as-burnt and the calcined samples at 600 and 800 ^{o}C respectively (Table 3).

Table 3. Average crystallite size and particle size of $Co_{0.5}Ni_{0.5}Fe_2O_4$ nanoferrites for (a) as-burnt (b) calcined sample at 600 ^{o}C and (c) calcined at 800 ^{o}C determined from XRD and FE-SEM.

Calcination temperature	as-burnt	600 ^{o}C	800 ^{o}C
D(nm) XRD	43.672	47.943	61.795
D(nm) FE-SEM	51.564	58.092	86.020

The increase in particle size with the increase of the calcination temperature may suggest the fusion of several neighboring particles together, which leads to an increase in particle size by melting their surfaces [16]. Fig 3-c shows a relatively uniform distribution of some aggregations and semi-spherical shapes of $Co_{0.5}Ni_{0.5}Fe_2O_4$ calcined at 800 ^{o}C.

Fig. 4 (a-c) shows an EDS spectrum of the investigated samples. The analysis of these spectra indicates the formation of the wanted oxide materials, suggesting that the mixed oxides have undergone the chemical reaction. The final product showed a completely removal of undesired precursor materials like nitrates ions. The energy dispersive spectrum for all samples evidences the spinel phase and the homogeneous composition of each powder sample.

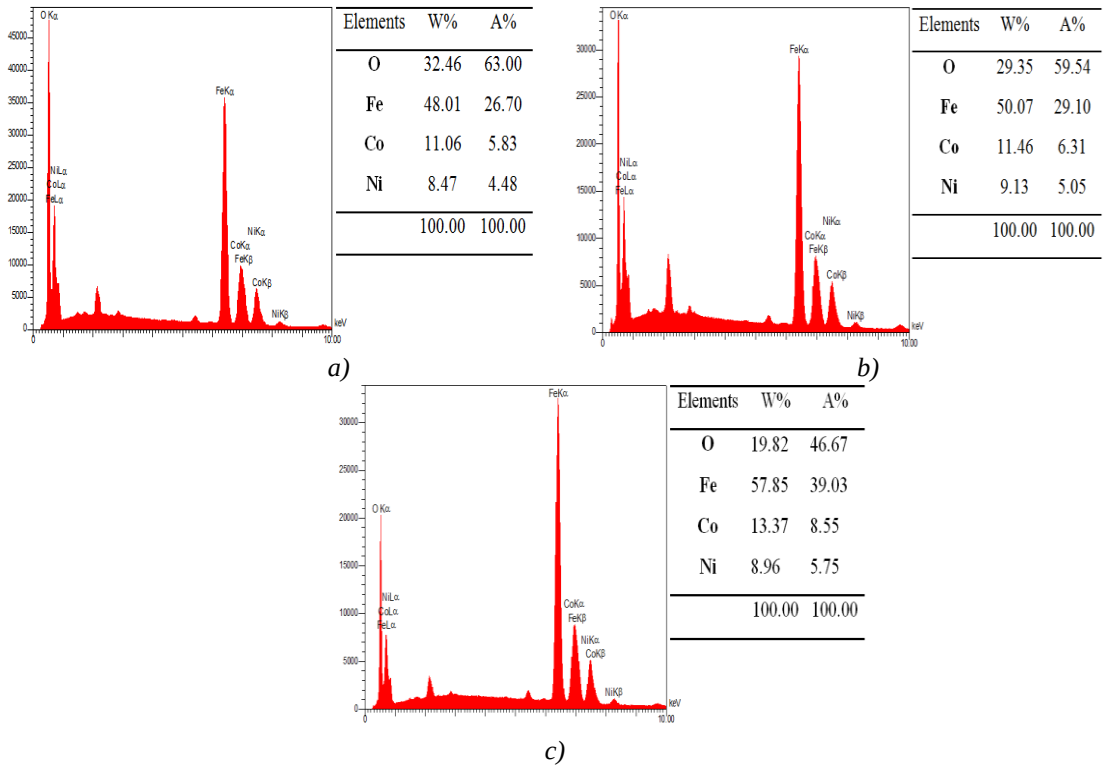

Fig. 4. EDS spectra of $Co_{0.5}Ni_{0.5}Fe_2O_4$ nanoferrites for (a) as-burnt (b) calcined sample at 600 ^{o}C and (c) calcined at 800 ^{o}C.

3.5. Optical properties

The reflectance measurement at room temperature is of great significance in optoelectronics application especially to study the optical band-gap energy [15]. Fig.5 (a-e) illustrates the optical band-gap energy variation for synthesized ferrites nanoparticles as a function of the calcination temperature. Tauc relation has been used for measuring the band-gap energy (E_g)

of the powder samples [18]. Herein, a graph is plotted between $(\alpha hv)^2$ vs. (hv), where α is the absorption coefficient and hv is the photon energy. Using Kumar model, the absorption coefficient α is proportional to the $ln[(R_{max}-R_{min})/(R-R_{min})]$, where reflectance falls from R_{max} to R_{min} due to the absorption by the powder samples, R is the reflectance for any intermediate energy photons [19, 20]. The linear part of the curve was extrapolated to $(hv\ ln[(R_{max}-R_{min})/(R-R_{min})])^2=0$ to get the direct band-gap energy.

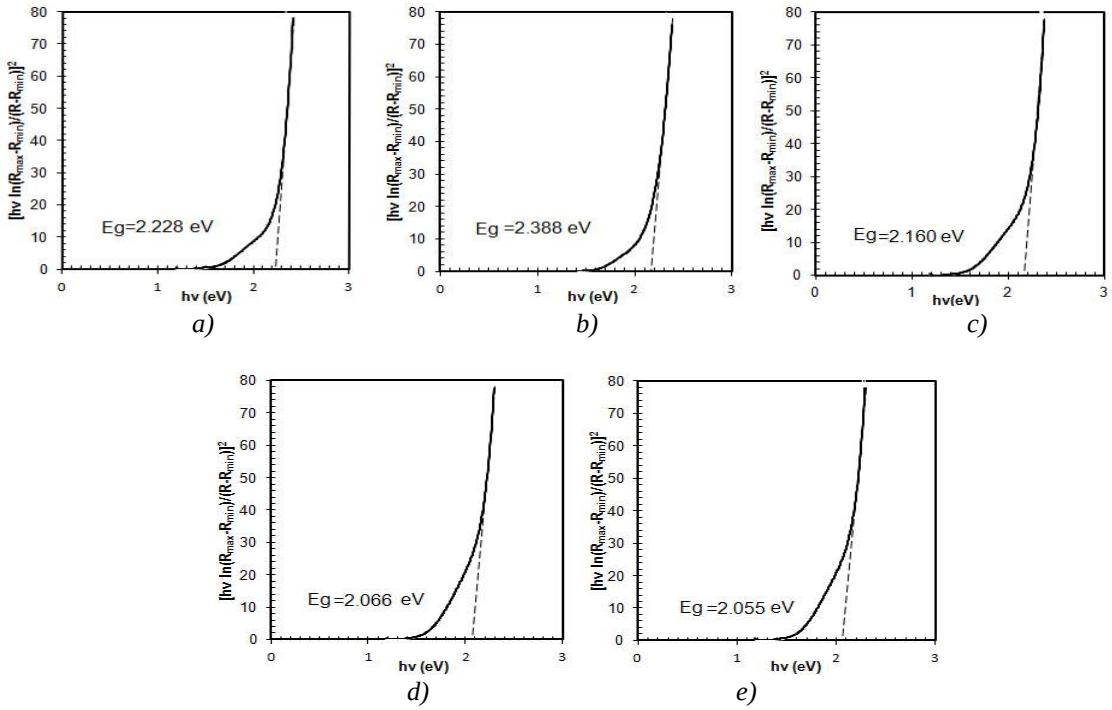

Fig. 5. Optical band-gap energy of $Co_{0.5}Ni_{0.5}Fe_2O_4$ nanoferrites for different calcination temperature (a) as-burnt (b) 500 °C, (c) 600 °C, (d) 700 °C, and (d) 800 °C.

From Fig. 5 (a-e), it was observed that the optical band-gap energy of $Co_{0.5}Ni_{0.5}Fe_2O_4$ nanoparticles tends to decrease as the particle size increases (Table 4). The energy decreases from 2.388 to 2.055 eV with the increase of the calcination temperature. The $Co_{0.5}Ni_{0.5}Fe_2O_4$ ferrite nanoparticles calcined at 800 °C temperatures showed a bigger size with a wider distribution of particle size and also lower band-gap energy. This behavior can be understood as follows; as the atomic vibration amplitude increases due to the increase in the thermal energy, there occurs an increase in the interatomic spacing as well. The increase of interatomic spacing leads to the decrease in the average potential seen by the electrons in the material, which minimizes the energy band-gap size [21]. The estimated band-gap energy is in good agreement with those reported by other research groups of ZnO and CeO_2 [22, 23],and within the range reported for ferrites powder [24, 25].

Table 4. Values of band-gap energy (Eg) of $Co_{0.5}Ni_{0.5}Fe_2O_4$ nanoferrites for different calcination temperature.

***Temp.* °C**	***Eg*(eV)**
as-burnt	2.388
500	2.228
600	2.160
700	2.066
800	2.055

3.5. Magnetic studies

Fig. 6 demonstrates the magnetic hysteresis loops measured at room temperature under an applied magnetic field of -15 to +15 KOe. All samples display various properties after calcination at different temperatures.

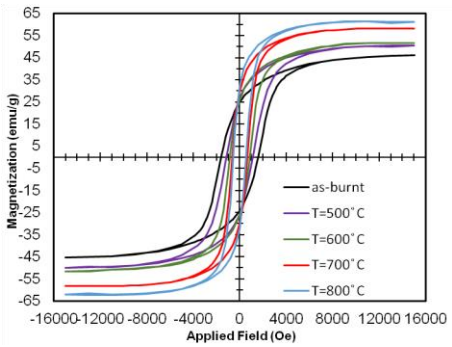

Fig. 6. Hysteresis loops of $Co_{0.5}Ni_{0.5}Fe_2O_4$ nanoparticles for different calcination temperature

All the synthesized ferrite samples exhibit ferrimagnetic behavior. The values of the saturation magnetization (M_S), remanance magnetization (M_r), and coercivity (H_c) are obtained from the hysteresis loops. The experimental magnetic moment (n_B), squareness ratio (S), and magnetic anisotropy (K) are evaluated from the following relations respectively [26].

$$n_B = \frac{(M_{wt} \times M_s)}{5585} \tag{6}$$

$$Remnance\ ratio = \frac{M_r}{M_s} \tag{7}$$

$$H_c = \frac{(0.96 \times K)}{M_s} \tag{8}$$

where, M_{wt} is the molecular weight

It can be seen that the values of saturation and remanance magnetization increase with the increase of the calcination temperature. The saturation magnetization (M_S) of as-burnt sample (lower temperature) had a value of 46.1291emu/g. While samples with higher calcination temperature of 500, 600, 700 and 800 °C had M_S values of 50.5922, 51.6639, 58.1878 and 61.5354 emu/g, respectively, as indicated in Table 5.

Table 5. Variation in saturation magnetization (M_s), remanance magnetization (M_r), coercivity (H_c) magnetic moment (n_B), squareness ratio (M_r/M_s), and magnetic anisotropy (K) of $Co_{0.5}Ni_{0.5}Fe_2O_4$ nanoferrites for different calcination temperature.

***Temp.* °C**	M_s **(emu g^{-1})**	M_r **(emu g^{-1})**	H_c **(Oe)**	n_B **(μ_B)**	M_r/M_s	$K \times 10^3$ **(emu · O$_e$ g^{-1})**
as-burnt	46.1291	24.9429	1595.00	1.94	0.54	76.64
500	50.5922	25.2833	1111.00	2.12	0.50	58.55
600	51.6639	28.7122	863.19	2.17	0.56	46.45
700	58.1878	29.8258	663.87	2.44	0.51	40.24
800	61.5354	32.4041	558.15	2.58	0.53	35.78

The change in saturation magnetization with the calcination temperature may be due to spin canting and disorder in the surface spin that take place in these nanoparticles [27]. Similar observations were also perceived on other spinel ferrite nanoparticles by M. G. Naseri et al. [27]. The sample that calcined at 800 °C, has a higher crystallite size, and exhibits a higher magnetic moment compared with the other samples. This is probably related to the crystallite size and surface/volume ratio [28]. Aslibeiki et al. [29] also reported that an increase in the saturation magnetization with the calcination temperature is attributable mainly to the growing of crystallite size and the crystallinity of samples. B. Purnama et al. [30] demonstrated that Fe^{3+} ions have a higher magnetic moment compared to that of Co^{2+} ions, which leads to the redistribution of dominant Fe^{3+} ions at B sites. Hence, the total magnetic moment number will increase and as a result the saturated magnetization in the cobalt ferrite nanoparticles will increase.

The coercivity values (H_c**)** of all ferrite samples decrease with the increase of the calcination temperature. Generally, the magnetization or demagnetization produced by domain wall movement needs lower energy and the increase in crystallite size brings about elevation in the number of walls. The magnetization or demagnetization produced by the wall movement is larger than that of single-domain rotation. Therefore, the samples with higher calcination temperature are expected to have a lower coercivity [31]. Abdallah et al. [32] reported that the large coercive values at low temperatures are correlated with the increase of the effective anisotropy field. According to Néel's two sublattice model, the individual magnetic moments of A and B-sub-lattice have aligned anti-parallel (opposite direction) with each other and their spins have a collinear structure. Therefore, the total magnetization is ($M = M_B - M_A$) and the A-sublattice magnetization is lower compared to the B-sublattice [26]. In this study, the magnetic moment variation with grain size can also be explained according to the cation distribution and the intensity of the super-exchange interaction between the ions on the A and B-sub-lattice. The squareness ratio (S) determines the magnetic hardness of the material, which is dependent on the anisotropy of the system. The amount of squareness determines whether or not the inter-grain exchanges occur [33]. Ali et al, [9] have reported when the (S) < 0.5 the particles interact by magneto-static interactions and exchange-coupled interaction survives when (S) >0.5. Our results elucidate that the values of (S) are approximately larger than 0.5. Therefore, the nanoparticles have exchange-coupled interaction.

4. Conclusions

$Co_{0.5}Ni_{0.5}Fe_2O_4$ ferrite nanoparticles were successfully synthesized using sol-gel auto combustion method. The effect of calcination temperature on crystallinity, phase composition, morphology, optical and magnetic properties was investigated by various characterization methods, i.e., XRD, FT-IR, FE-SEM DRS, and VSM respectively. XRD and FT-IR displayed that all samples exhibited the characteristic behavior of cubic spinel ferrite nanoparticle. The crystallite size, lattice parameter, x-ray density, and hopping length were found to be dependent on the calcination temperature. EDS is used to study the composition characterization and confirmed the presence of Co, Ni, Fe, and O in all samples. FE-SEM images clearly showed that the grain size increases as the calcination increases.

The influence of calcination temperature on band-gap energy was studied by DRS, and it was found that all samples have a direct band-gap increase with the increase of both the calcination temperature and the particle size. Magnetization measurement indicated that an increase in the calcination temperature elevates the saturation magnetization, remanance magnetization, and magnetic moment. Moreover, higher calcination displays higher crystallite size, higher saturation magnetization and magnetic moment compared with the lower calcination temperature, and this is due to their high degree of crystallization and uniform morphologies. The sample that calcined at 800 °C, had a higher crystallite size, and exhibited a higher magnetic moment. This is probably related to the crystallite size and surface/volume ratio.

References

[1] M. Raghasudha, D. Ravinder, P. Veerasomaiah, Journal of Nanostructure in Chemistry **3**(63), 1 (2013).
[2] B. Toksha, S. E. Shirsath, S. Patange, K. Jadhav, Solid State Communications **147**(11-12), 479 (2008).
[3] M. Hashim, S. Kumar, S. E. Shirsath, R. Kotnala, J. Shah, R. Kumar, Materials Chemistry and Physics **139**(2-3), 364 (2013).
[4] S. Maensiri, C. Masingboon, B. Boonchom, S. Seraphin, Scripta materialia **56**(9), 797 (2007).
[5] C. C. Naik, A. Salker, Journal of Superconductivity and Novel Magnetism, 1 (2019).
[6] R. Sagayaraj, S. Aravazhi, G. Chandrasekaran, SN Applied Sciences **1**(271), 2019.
[7] Z. Rouhani, J. Karimi-Sabet, M. Mehdipourghazi, A. Hadi, A. Dastbaz, Environmental Nanotechnology, Monitoring & Management **11**, 100198 (2019).
[8] M. Asif, M. Nadeem, M. Imran, S. Ahmad, S. Musaddiq, W. Abbas, Z. A. Gilani, M. K. Sharif, M. F. Warsi, M. A. Khan, Physica B: Condensed Matter **552**, 11 (2019).
[9] A. Mohammad, S. Ridha, T. Mubarak, Digest Journal of Nanomaterials and Biostructures **13**(8), 615 (2018).
[10] A. M. Mohammad, S. M. A. Ridha, T. H. Mubarak, International Journal of Applied Engineering Research 13(8), 6026 (2018).
[11] D. S. Nikam, S. V. Jadhav, V. M. Khot, R. Bohara, C. K. Hong, S. S. Mali, S. Pawar, RSC Advances 5(3), 2338 (2015).
[12] S. Maensiri, M. Sangmanee, A. Wiengmoon, Nanoscale research letters **4**(3), 221 (2009).
[13] M. Khandekar, R. Kambale, J. Patil, Y. Kolekar, S. Suryavanshi, Journal of Alloys and compounds **509**(5), 1861 (2011).
[14] A. Pradeep, P. Priyadharsini, G. Chandrasekaran, Journal of Magnetism and Magnetic Materials **320**(21), 2774 (2008).
[15] M. Azim, M. Chaudhry, N. Amin, M. Arshad, M. Islam, S. Nosheen, M. Ahmad, H. Anwar, M. Waseem, G. Mustafa, Digest Journal of Nanomaterials and Biostructures **11**(3), 953 (2016).
[16] M. Chireh, M. Naseri, Advanced Powder Technology **30**(5), 952 (2019).
[17] A. Druc, A. Dumitrescu, A. Borhan, V. Nica, A. Iordan, nd M. Palamaru, Open Chemistry **11**(8), 1330 (2013).
[18] Z. T. Khodair, M. A. Al-Jubbori, A. M. Hassan, M. S. Aljuboori, F. I. Sharrad, Journal of Electronic Materials **48**(1), 669 (2019).
[19] V. Kumar, T. Sharma, Optical Materials **10**(4), 253 (1998).
[20] V. Kumar, S. K. Sharma, T. Sharma, V. Singh, Optical materials **12**(1), 115 (1999).
[21] S. Panda, Microelectronics and optoelectronics technology: Laxmi Publications, New Delhi, 2009.
[22] U. Manzoor, M. Islam, L. Tabassam, S. U. Rahman, Physica E: Low-dimensional Systems and Nanostructures **41**(9), 1669 (2009).
[23] S. Maensiri, C. Masingboon, P. Laokul, W. Jareonboon, V. Promarak, P. L. Anderson, S. Seraphin, Crystal growth & design **7**(5), 950 (2007).
[24] R. Köferstein, T. Walther, D. Hesse, S. G. Ebbinghaus, Journal of materials science **48(**19), 6509 (2013).
[25] V. S. Kiran, S. Sumathi, Journal of Magnetism and Magnetic Materials **421**, 113 (2017).
[26] R. S. Yadav, I. Kuřitka, J. Vilcakova, J. Havlica, J. Masilko, L. Kalina, J. Tkacz, J. Švec, V. Enev, M. Hajdúchová, Advances in Natural Sciences: Nanoscience and Nanotechnology, **8**(4), 045002 (2017).
[27] M. G. Naseri, E. B. Saion, H. A. Ahangar, M. Hashim, A. H. Shaari, Journal of Magnetism and magnetic Materials **323**(3), 1745 (2011).
[28] S. Da Dalt, A. Takimi, T. Volkmer, V. Sousa, C. Bergmann, Powder technology **210**(2), 103 (2011).
[29] B. Aslibeiki, P. Kameli, H. Salamati, M. Eshraghi, T. Tahmasebi, Journal of Magnetism and Magnetic Materials **322**(19), 2929 (2010).
[30] B. Purnama, A. T. Wijayanta, Journal of King Saud University-Science, 2018.

[31] N. Kannapiran, A. Muthusamy, P. Chitra, S. Anand, R. Jayaprakash, Journal of Magnetism and Magnetic Materials **423**, 208 (2017).
[32] H. M. Abdallah, T. Moyo, N. Ngema, Journal of Magnetism and Magnetic Materials **394**, 223 (2015).
[33] N. Adeela, U. Khan, M. Iqbal, S. Riaz, M. Irfan, H. Ali, K. Javed, I. Bukhtiar, K. Maaz, S. Naseem, Journal of Alloys and Compounds **686**, 1017 (2016).